19th Brazilian Congress of Thermal Sciences and Engineering
November 6th–10th, 2022, Bento Gonçalves - RS - Brazil

ENC-2022-0188
NUMERICALLY ASSESSING THE IMPACT OF DIFFERENT HYPERELASTIC LAWS ON THE MECHANICAL RESPONSE OF INTRACRANIAL ANEURYSMS WALLS

Iago Lessa de Oliveira
São Paulo State University (UNESP), School of Engineering, Ilha Solteira, São Paulo, Brazil
iago.oliveira@unesp.br

Carlos Eduardo Baccin
Interventional Neuroradiology/Endovascular Neurosurgery, Beth Israel Deaconess Medical Center, Harvard Medical School, Boston, MA, US
cebaccin@gmail.com

José Luiz Gasche
São Paulo State University (UNESP), School of Engineering, Ilha Solteira, São Paulo, Brazil
jose.gasche@unesp.br

Abstract. *Intracranial aneurysms (IAs), a dangerous disease with up to 50 % mortality rate in case of rupture, is characterized as a dilatation of the cerebral arteries and, biologically, their walls fit within the class of soft tissues. Numerical studies on the rupture of an IA have become increasingly popular, but the correct constitutive law of its wall tissue, normally assumed to be an incompressible hyperelastic material, is essential to provide meaningful results. A couple of hyperelastic laws were already used to investigate IAs wall motion by a few works, and no answer on the most suitable one exists. Hence, in this work, we investigated the effect of different laws on the mechanical response of patient-specific IAs. Pulsatile numerical simulations were carried out using the one-way fluid-solid interaction solution strategy implemented in solids4foam, in which the blood flow is solved and applied as the driving force of the wall motion, with the geometries of two patient-specific IA, obtained from medical examinations. The IA and artery walls were assumed isotropic and their thickness and material properties were computationally created with realistic modeling and using IA tissue experimental data. The Yeoh law, the three-parameter Mooney-Rivlin (MR) law, and a Fung-like law with a single parameter, typically used for soft tissues, were employed to assess the influence of different laws. The results suggest that the effect of different hyperelastic laws is larger for the stretch than the stress. Additionally, both stress and stretch decreased along the wall thickness. These results could guide modeling decisions on IA simulations.*

Keywords: *intracranial aneurysms, aneurysm wall constitution, hyperelasticity, solids4foam*

1. INTRODUCTION

Intracranial aneurysms (IAs) are pathological dilatations with saccular shape of the human vascular system normally found in the bifurcations of the cerebral arteries tree. It is a dangerous disease with up to 50 % mortality rate in case of rupture (Vlak *et al.*, 2013; Saqr *et al.*, 2019). The problem is that rupture is hard to predict and treatments pose risk to patients, leaving physicians with a tough decision about the treatment. Enhanced ways to predict the rupture have occupied researchers for the past two decades, and one of the most used techniques to, at least, understand the disease progression and final rupture employed numerical tools, such as Computational

Fluid Dynamics (CFD) (Liang *et al.*, 2019). Currently, the practical use of numerical techniques to assess the likelihood of IA rupture is a debated topic in the literature (Kallmes, 2012; Cebral and Meng, 2012).

Nevertheless, they can be helpful because numerical techniques such as Computational Solid Dynamics (CSD) and computational Fluid-Solid Interaction (FSI) can predict the stresses and strain in the wall of a patient-specific IAs. However, when modeling an IA wall tissue, a difficulty is the lack of patient-specific data of the wall morphology, such as its thickness, and mechanical properties, such as the tissue constitutive law and its material properties. This is particularly important due to the large variability of the disease.

Regarding the selection of the constitutive law, researchers that numerically solved the FSI problem with patient-specific IA subjects have used several different laws. Surprisingly, we found a majority that has chosen the small-strain Hookean law that, rigorously, should not be used in finite-deformation motions (Torii *et al.*, 2006; Valencia *et al.*, 2009; Lee *et al.*, 2013; Cho *et al.*, 2020). Other authors employed the classic neo-Hookean law (Bazilevs *et al.*, 2010b) or more specialized ones, such as exponential laws (Torii *et al.*, 2008) and the Mooney-Rivlin (MR) law (Sanchez *et al.*, 2014), although in a smaller number, and not always using the material properties of patient-specific IA tissue.

Furthermore, the assessment of the impact of different material laws on the mechanics of IAs walls has been the subject of even fewer studies (Torii *et al.*, 2008; Ramachandran *et al.*, 2012). In this current scenario, it remains broadly unknown what is the impact of the use of different hyperelastic laws in the mechanics of IAs, i.e. in the stress and strain fields of the IA sac. Therefore, the aim of this work is to assess the impact of different constitutive laws on the mechanical response of IAs. Furthermore, we have employed recently acquired experimental data on the mechanical properties of IA tissue (Costalat *et al.*, 2011; Brunel *et al.*, 2018).

2. NUMERICAL METHODOLOGY

2.1 Geometries Reconstruction

The images of two patient-specific IAs, one ruptured and one unruptured, were obtained from medical examinations: the unruptured case was collected in the Albert Einstein Israelite Hospital (approved to be used by the ethical committees of the institutions involved) and the ruptured case was taken from the Aneurysk repository (Passerini *et al.*, 2021) (available under the "CC BY-NC 3.0" license). The images were then segmented using the Vascular Modeling Toolkit (VMTK)® library with the level-sets segmentation approach (Piccinelli *et al.*, 2009). The geometries of both IAs are shown in Fig. 1.

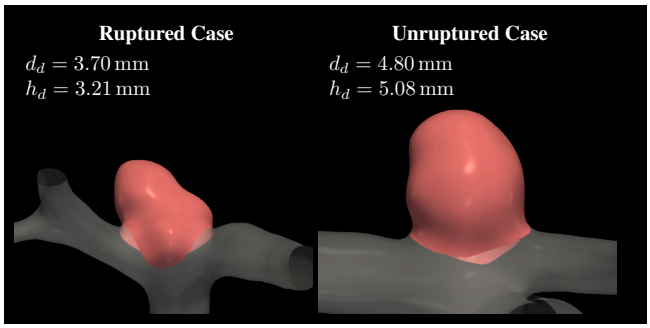

Figure 1. Geometries of the IAs: the ruptured case (left) and the unruptured case (right), with the necks delineated and showing the maximum sac height (h_d), and the maximum sac diameter (d_d).

2.2 Physical and Mathematical Modeling and Boundary Conditions

We employed a strategy called "one-way fluid-solid interaction (1WFSI)" to numerically solve for the interaction between the blood flow and the solid wall motion (Hirschhorn *et al.*, 2020). By using this technique, the fluid flow is solved by assuming a rigid interface between the flow and the solid (FSI interface) with the typical CFD boundary conditions (BCs) for walls — zero mass flux, zero pressure gradient, and the no-slip condition. Then, at each instant in time, the traction on this interface, due to the blood flow is transferred to the solid FSI interface counterpart and applied as traction BCs to the solid problem. The resulting solid deformation

is not transferred back to the fluid domain. The coupling then is unidirectional and this method was chosen to avoid the numerical instabilities that arise in the numerical solution of flow in arterial geometries. See Fig. 2 for a schematic illustration of the FSI interface of a vascular geometry and the BCs applied. The fluid flow and solid models are described in the following.

Blood Flow Model

Blood is a weakly compressible fluid (Sacks and Tickner, 1968) and was assumed as such by using a compressible equation of state and the Newtonian contitutive law to represent it, flowing in an isothermal laminar regime. Hence, the governing equations solved were the continuity equation:

$$\frac{\partial}{\partial t}\left(\int\limits_{V^{\mathrm{f}}} \rho^{\mathrm{f}} \mathrm{d}V\right) + \oint\limits_{S^{\mathrm{f}}} \rho^{\mathrm{f}} \boldsymbol{v}^{\mathrm{f}} \bullet \boldsymbol{n}^{\mathrm{f}} \mathrm{d}S = 0\,, \tag{1}$$

where $\boldsymbol{v}^{\mathrm{f}}$ is the flow velocity, ρ^{f} is the blood density, and $\boldsymbol{n}^{\mathrm{f}}$ is the outward normal vector to the control surface S^{f}; and the momentum equation:

$$\frac{\partial}{\partial t}\left(\int\limits_{V^{\mathrm{f}}} \rho^{\mathrm{f}} \boldsymbol{v}^{\mathrm{f}} \mathrm{d}V\right) + \oint\limits_{S^{\mathrm{f}}} \rho^{\mathrm{f}} \boldsymbol{v}^{\mathrm{f}} \boldsymbol{v}^{\mathrm{f}} \bullet \boldsymbol{n}^{\mathrm{f}} \mathrm{d}S = \oint\limits_{S^{\mathrm{f}}} \boldsymbol{\sigma}^{\mathrm{f}} \bullet \boldsymbol{n}^{\mathrm{f}} \mathrm{d}S\,, \tag{2}$$

where $\boldsymbol{\sigma}^{\mathrm{f}}$ is the Cauchy stress tensor, given by:

$$\boldsymbol{\sigma}^{\mathrm{f}} = -p^{\mathrm{f}} \boldsymbol{I} + \mu^{\mathrm{f}} \left[\nabla \boldsymbol{v}^{\mathrm{f}} + (\nabla \boldsymbol{v}^{\mathrm{f}})^{\mathrm{T}}\right] - \frac{2}{3}\mu^{\mathrm{f}} \left(\nabla \bullet \boldsymbol{v}^{\mathrm{f}}\right) \boldsymbol{I}\,, \tag{3}$$

with p^{f} being the flow pressure and $\boldsymbol{I}$ the second-order identity tensor. Blood dynamic viscosity was assumed to be $\mu^{\mathrm{f}} = 3.3 \times 10^{-3}\,\mathrm{Pa\,s}$. Additionally, the compressibility of blood was assumed to be governed by the barotropic equation of state (Kanyanta, 2009; Kanyanta *et al.*, 2009), by which the pressure and the fluid density are linearly related:

$$\rho^{\mathrm{f}} = \rho_0^{\mathrm{f}} + \frac{\rho_0^{\mathrm{f}}}{\kappa^{\mathrm{f}}} \left(p^{\mathrm{f}} - p_0^{\mathrm{f}}\right)\,, \tag{4}$$

where κ^{f} is the bulk modulus of blood, assumed to be $2.2 \times 10^9\,\mathrm{Pa}$ (Kanyanta, 2009), and the subscript "0" indicates a reference state of the fluid, assumed to be blood at an average cardiac cycle pressure, 100 mmHg, with $\rho_0^{\mathrm{f}} = 1000.0\,\mathrm{kg/m^3}$.

Regarding the flow BCs, at the flow inlet (see Fig. 2a), a time-varying pulsatile velocity profile was imposed, varying spatially according to the fully-developed laminar flow in a pipe:

$$\boldsymbol{v}_{inlet}^{\mathrm{f}}(r,t) = 2\frac{q_a(t)}{A_{inlet}} \left[1 - \frac{4r^2}{{d_a}^2}\right]\,, \tag{5}$$

where A_{inlet} is the cross-sectional area of the inlet artery, d_a is its inner diameter, and r is the radial coordinate of the circular inlet section — an artificial circular-section extension, with a length equal to twice the diameter d_a, was added to the artery inlet to impose this inlet flow condition. The blood flow rate, $q_a(t)$, corresponding to the flow pulse from the beginning of systole until the end of the diastole, was obtained by multiplying the normalized flow rate reported by Hoi *et al.* (2010), for older adults, by the mean blood flow rate in the respective IA parent artery reported by Zarrinkoob *et al.* (2015). This population-averaged rate was employed because the patient-specific blood flow rate waveform at the internal carotid artery (ICA) was not available. An example of the profile used for IAs on the ICA is shown in Fig. 2b. Moreover, the pressure gradient was set to zero at the inlet.

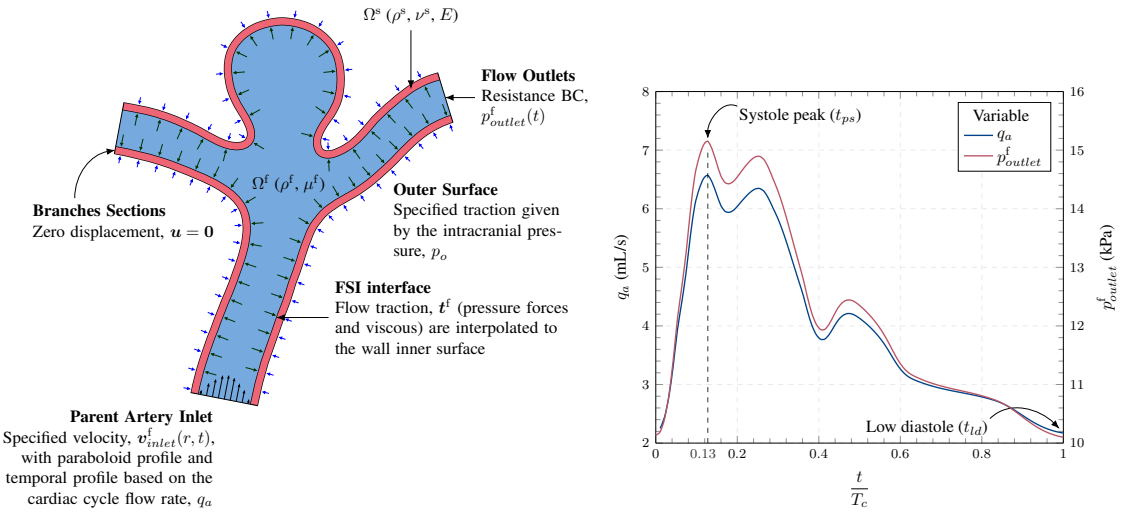

(a) (b)

Figure 2. (a) Schematic two-dimensional representation of the BCs applied in the aneurysms 1WFSI simulations; (b) the blood flow rate and pressure waveform used in the inlet and outlets, respectively.

IAs and Arterial Wall Model

The IA and artery walls were assumed isotropic and nearly incompressible, thus the momentum equation in the total Lagrangian formulation was solved, written as:

$$\rho_0^{\mathrm{s}} \frac{\partial^2 \boldsymbol{u}}{\partial t^2} = \nabla_0 \bullet \left[J \boldsymbol{F}^{-1} \bullet \left(\boldsymbol{\sigma}^{\mathrm{s}} + \boldsymbol{\sigma}_0^{\mathrm{s}} \right) \right] , \tag{6}$$

where $\boldsymbol{u}$ is the solid displacement, ρ_0^{s} is the solid density at the reference configuration, $\boldsymbol{F} = \boldsymbol{I} + (\nabla_0 \boldsymbol{u})^{\mathrm{T}}$ is the deformation gradient, and $J = \det(\boldsymbol{F})$. The subscript "0" indicates any property or derivative taken with respect to the reference configuration, assumed to be the domain configuration at the time zero and with prestress given by $\boldsymbol{\sigma}_0^{\mathrm{s}} = J^{-1} \boldsymbol{F} \bullet \boldsymbol{S}_0 \bullet \boldsymbol{F}$. The second Piola-Kirchhoff prestress tensor, $\boldsymbol{S}_0$, was computed prior to solving Eq. (2) using the same approach employed by Bazilevs *et al.* (2010a).

The Cauchy stress of the solid, $\boldsymbol{\sigma}^{\mathrm{s}}$, was calculated using three different hyperelastic laws that are defined based on their strain-energy function, Ψ, as follows: (1) the MR law with 3 material constants (Mooney, 1940):

$$\Psi(I_1, I_2) = c_{10} (I_1 - 3) + c_{01} (I_2 - 3) + c_{11} (I_1 - 3)(I_2 - 3) \ ; \tag{7}$$

the Yeoh law with 3 material constants:

$$\Psi(I_1) = c_{10} (I_1 - 3) + c_{20} (I_1 - 3)^2 + c_{30} (I_1 - 3)^3 \ ; \tag{8}$$

and an "isotropic" version of the exponential Fung-like law, originally proposed by Demiray (1972):

$$\Psi(I_1) = \frac{k_1}{k_2} \left[\mathrm{e}^{\frac{k_2}{2}(I_1 - 3)} - 1 \right] , \tag{9}$$

where I_1 and I_2 are the first and second invariants of the right Cauchy-Green deformation tensor, $\boldsymbol{C} = \boldsymbol{F}^{\mathrm{T}} \bullet \boldsymbol{F}$. The complete constitutive law employed a volumetric-decomposition approach as explained in Holzapfel *et al.* (2000). In this framework, the volumetric part of the tissue motion, dependent on the tissue compressibility, is ultimately measured by the Poisson's ratio of the tissue, ν^{s}, through its bulk modulus, κ^{s}, as computed by the linearized theory:

$$\kappa^{\mathrm{s}} = \frac{E}{3(1 - 2\nu^{\mathrm{s}})} , \tag{10}$$

where the linearized Young's modulus for the hyperelastic laws was calculated based on the uniaxial deformation, resulting in $E = 6\left(\frac{\partial \Psi}{\partial I_1} + \frac{\partial \Psi}{\partial I_2}\right)$ (Holzapfel, 2000). We assumed a Poisson ratio of 0.48, which was defined after a parametric study of its influence on the stresses and stretch on an IA sac surface — larger values of ν^{s}, i.e. values closer to the incompressibility limit, changed the averaged stretch and stress fields over the sac by less than 2 %, for all the hyperelastic laws, while still yielding reasonable computational times.

The properties of the vascular wall, i.e. its thickness, e_w, and material constants, c_{ij}, were modeled using a heterogeneous model with different properties on the branches and on the aneurysm sac. The creation of this model depends on the delineation of the *neck contour*, which was carried out by manually selecting it on the triangulated surface extracted from the image examinations using VMTK® (see Fig. 1). Mathematically, the neck contour separates the surface of the branches, S_b, from the IA sac, S_{ia} (see Fig. 3 for a schematic example of the neck contour and other terms used in this section).

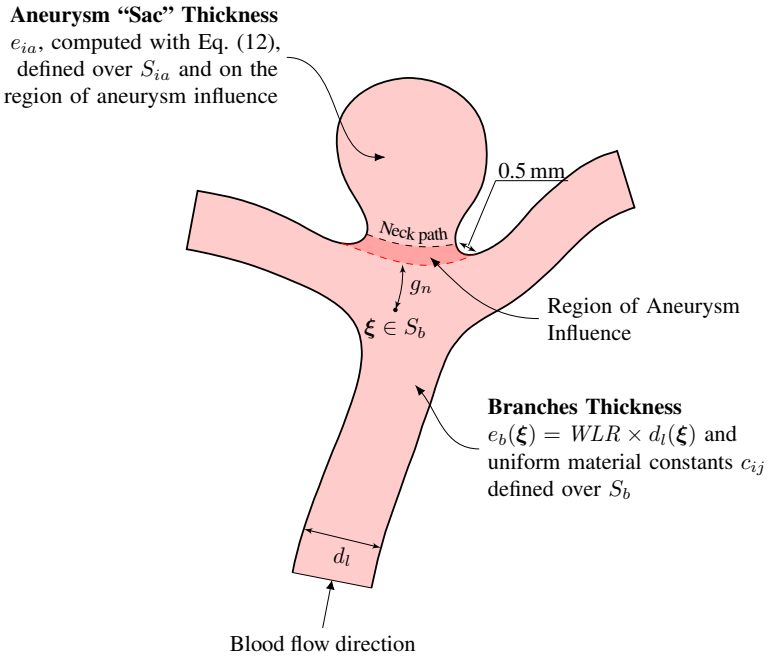

Figure 3. Schematic illustration of the morphology model components: the branches surface has a lumen diameter-dependent thickness and uniform material constants, while the aneurysm sac has a "sac" uniform thickness and uniform material constants.

We assumed the material constants, c_{ij}, as uniform on both S_b and S_{ia}, but with different values according to the rupture status, following experimental evidence that the tissue of unruptured IAs is stiffer than ruptured IAs tissue (Costalat *et al.*, 2011). Hence, the values for each constant (see Table 1) were based on averages of experimental data provided by Costalat *et al.* (2011); Brunel *et al.* (2018) and values used by Torii *et al.* (2010).

The thickness of S_b, e_b, was based on established evidence that the thickness of arteries is dependent on the vessel lumen diameter (Fung, 1993). Thus, it was calculated as $e_b = WLR \times d_l$ (see Fig. 3), where d_l is the artery's lumen diameter at a specified position along the vasculature, estimated by computing the distance between the vasculature *centerlines* and its surface using VMTK (Piccinelli *et al.*, 2009), and WLR is the wall-to-lumen ratio (WLR) reported by Nakagawa *et al.* (2016) for the cerebral arteries. We used these reported values to define a functional form of WLR according to the lumen diameter, as follows:

$$WLR = \begin{cases} 0.070 & d_l < 2\,\mathrm{mm} \\ 0.070 + 0.018\,(d_l - 2) & 2\,\mathrm{mm} < d_l < 3\,\mathrm{mm} \\ 0.088 & d_l > 3\,\mathrm{mm} \end{cases} . \tag{11}$$

Based on the thickness field of the surrounding branches, we estimated the patient-specific uniform thickness

Table 1. Material constants selected for arteries branches, S_b, and for the IA sac, S_{ia}, according to rupture status, for different constitutive laws and based on experimental works by Costalat *et al.* (2011) and Brunel *et al.* (2018).

Law	Constant	S_b	S_{ia}	
			Ruptured	Unruptured
MR	c_{10} (MPa)	0.1966	0.19	0.19
	c_{01} (MPa)	0.0163	0.026	0.023
	c_{11} (MPa)	7.837	1.377	11.780
Yeoh	c_{10} (MPa)	0.1067	0.07	0.12
	c_{20} (MPa)	5.1602	2.10	6.80
	c_{30} (MPa)	0.0	0.0	0.0
Fung	k_1 (MPa)	0.3536	0.1768	0.7072
	k_2	16.7	16.7	16.7

of the IA sac, e_{ia}, as a weighted average, as follows:

$$e_{ia} = f_a \frac{\int_{S_b} g_n(\boldsymbol{\xi}) e_b(\boldsymbol{\xi}) \mathrm{d}S_b}{\int_{S_b} g_n(\boldsymbol{\xi}) \mathrm{d}S_b}, \tag{12}$$

where f_a is a factor to control how much thinner the aneurysm wall was compared to the vasculature; $f_a = 0.75$ was used consistently for all geometries to assure that the resulting thickness was within the range of measured thickness of IA walls (Costalat *et al.*, 2011). The weight function, g_n, is the minimum geodesic distance between each point of the surrounding branches, S_b, and the line that separates the sac and the *region of aneurysm influence* (see Fig. 3). This line may be imagined as a separation between the *hypothetical healthy vasculature* and the region of aneurysm influence. It was computed automatically as being 0.5 mm apart from the neck contour consistently for all geometries.

Computationally, these fields were built with scripts in VMTK® and an in-house code based on the Visualization Toolkit (VTK)®. This computational procedure created a discontinuity between the properties on S_{ia} and S_b. To correct this biologically unrealistic discontinuity, the resulting thickness was smoothed out using a script of VMTK® to smooth fields defined over surfaces — we employed fifteen iterations to remove the discontinuities.

Regarding the BCs, the inner surface, which coincides with the vascular lumen, was subjected to the traction forces from the flow, as described above due to the 1WFSI technique. On the outer (or abluminal) surface, a pressure of $p_o = 5\,\mathrm{mmHg}$, corresponding to the intracranial pressure, was imposed. Although the intracranial pressure seems to vary among patients, we have found similar values in related studies (Valencia *et al.*, 2013; Sanchez *et al.*, 2014). At the artificial "sections" made on the branches due to the segmentation (indicated in Fig. 2a), we imposed a fixed zero displacement or, mathematically, $\boldsymbol{u} = \mathbf{0}$.

2.3 Computational Meshes and Numerical Strategies

The computational meshes were built in foam-extend, with the cfMesh library, and the simulations were carried out in solids4foam, an extension of OpenFOAM® with the 1WFSI algorithm already implemented. The fluid flow mesh was generated using the utility `cartesianMesh`, which generates hexahedral-dominant meshes. Mesh-sensitivity studies for the fluid meshes were carried out extensively with different IAs geometries and yielded a volume density of cells in the range of 3000 to 4000 cells/m^{3}m. To generate the solid wall mesh, the external surface of the fluid mesh was "re-meshed" with only triangular cells and extruded in its outward direction with the thickness field e_w (see Fig. 3) using VMTK. We carried out a mesh-independence study of the solid meshes by also using the 1WFSI strategy with three systematically-refined meshes. The result was a mesh with a surface-cells density of approximately 240.0 cells/mm^2, with 6 layers of cells along the thickness. We also carried out a time-step refinement study yielding a time-step of 1×10^{-4} s.

For the fluid sub-problem, an adapted version of the Pressure Implicit with Splitting Operators (PISO) algorithm for weakly compressible fluids (Issa, 1986) was employed to solve the system of discretized equations, and a segregated algorithm was used to solve the solid sub-problem. Regarding the interpolation schemes, the central differences scheme was used for all the Laplacian terms, with non-orthogonal and skewness corrections (Jasak, 1996). Particularly for the flow momentum and pressure equations, the second-order upwind scheme was used for the advective term. Additionally, all the gradients in the equations were discretized with the least-squares scheme. The temporal discretization was performed by using the implicit Euler approach for the solid momentum equation and the implicit second-order Euler approach for the flow momentum equation. The normalized residual convergence criteria were: 1×10^{-6} for the flow pressure equation, 1×10^{-8} for the flow momentum equation, and 1×10^{-9} for the outer iterations of the solid momentum. Finally, two cardiac cycles were solved in each simulation, but only the second one was used for the analysis.

2.4 Data Analysis

We analyzed the fields of the largest principal Cauchy stress, σ_1, and largest principal stretch, λ_1. All the results were taken on the inner and outer surfaces of the wall (luminal and abluminal surfaces of the vasculature, respectively) taken at the peak systole instant, t_{ps}, and the results are shown in the reference configuration. Additionally, we also computed the surface average of σ_1 and λ_1 over S_{ia}, defined as follows, for σ_1:

$$\langle \sigma_1 \rangle_{S_{ia}} = \frac{1}{A(S_{ia})} \int_{S_{ia}} \sigma_1(\boldsymbol{\xi}) \mathrm{d}S_{ia} \,, \tag{13}$$

where $A()$ is the area operator.

3. RESULTS AND DISCUSSIONS

The results for the two IAs simulated suggest that hyperelastic laws affect λ_1 more than the σ_1 (see Figs. 4 and 5). More specifically, the isotropic Fung and Yeoh laws produced higher levels of stretch in much larger areas than the MR, whereas the σ_1 field is similar among all the laws, with small qualitative differences. Additionally, the overall levels of λ_1 are much larger for the ruptured case. Note that these observations regarding the overall fields also reflect on the surface average of the variables (annotated in the figures).

We found few studies that have also investigated the impact of different constitutive laws on the mechanical response of IAs in the past two decades. Torii *et al.* (2008) assessed the impact of different materials laws mainly on the hemodynamics, using a single IA geometry, thus limiting the possibility of comparison with our results (regarding the wall motion the authors only reported the maximum displacement on the IA sac and only used one law employed in this work, the Fung one). Ramachandran *et al.* (2012) directly compared different material laws in patient-specific IA geometries, although they assumed static BCs and simulated only the IA sac, i.e. without the branches walls. They employed anisotropic and isotropic versions of the Fung law, the Yeoh law, and both small and finite strain versions of Hooke's law. Although the material constants they have employed were different, their conclusions broadly agree that the material laws predicted similar responses in terms of the wall stresses. Although, it is important to note that they have not used the MR law, the one that presented the most divergent response compared to the Yeoh and Fung responses.

The observed similarity of σ_1 among all the laws further suggests that this field is indeed statically determined, one of the main questions raised by Ramachandran *et al.* (2012). This occurred irrespective of rupture status, hence further reinforcing that conclusion. On the other hand, λ_1 was more different according to the material law, hence, using a similar language, stretch (and, more generally, strain) is not statically determined and was subject to a significant influence of the material constants. In this regard, the larger levels of λ_1 in the rupture case could potentially represent an important indicator of rupture.

It is also possible to see in Figs. 4 and 5 that both σ_1 and λ_1 tend to decrease from the luminal to the abluminal surfaces, indicating that the harshest mechanical solicitations occur near the lumen — especially for σ_1, since the change is smaller for λ_1, as can be verified by comparing the surface averages. This behavior along the wall thickness is expected in this kind of geometry due to the boundary conditions applied on the inner and outer surfaces of the wall, i.e. relatively complex fields of wall shear stress (WSS) and pressure forces from the flow.

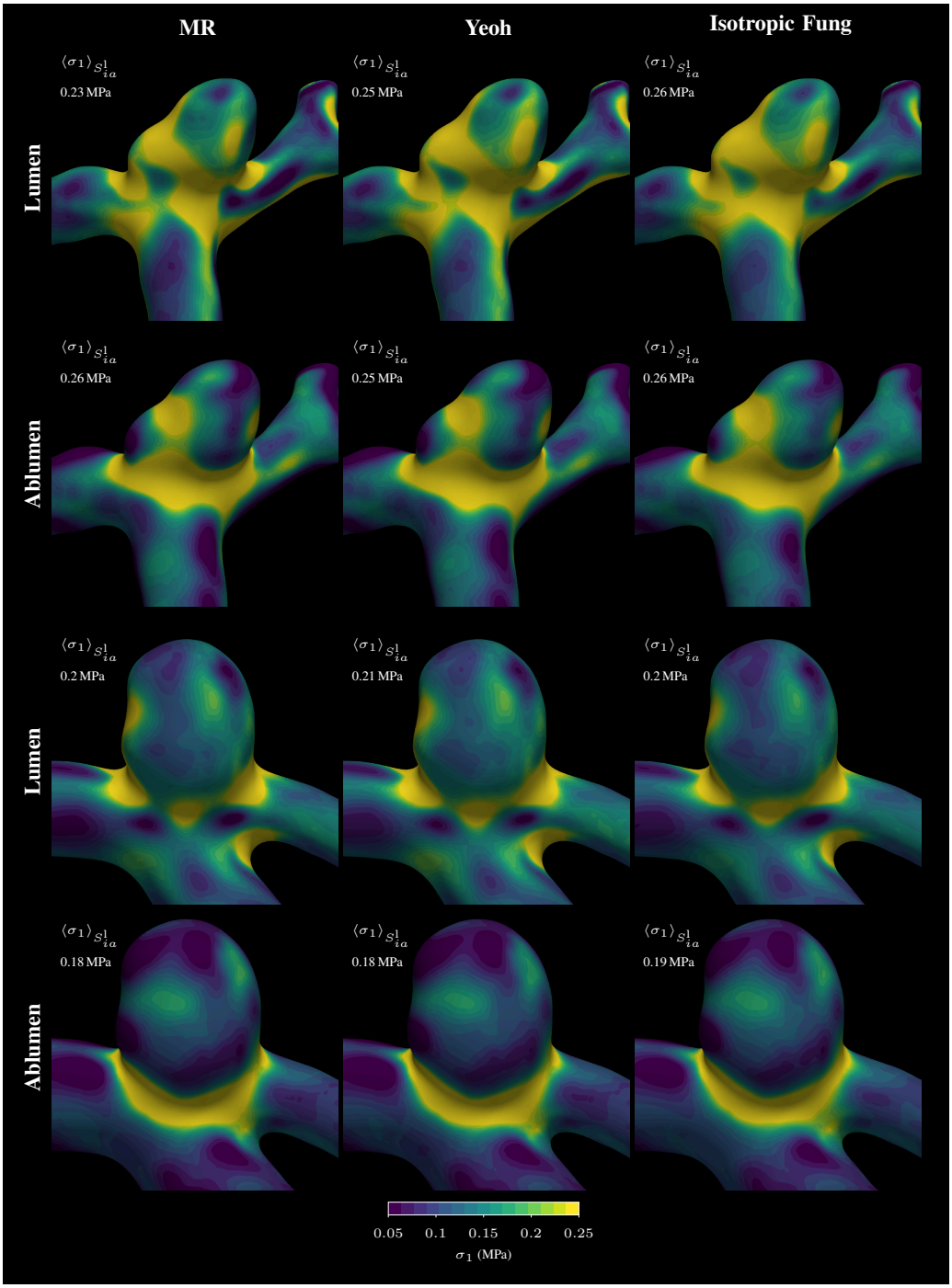

Figure 4. Largest principal Cauchy stress field at the peak systole, σ_1, on the luminal and abluminal surfaces of the wall, for the ruptured (top panel) and unruptured (bottom panel) cases, with different hyperelastic laws (columns).

Furthermore, although the variations along the thickness are relatively small, this behavior gives rise to normal and tangential gradients in the wall that could potentially have damaging effects on the structural integrity of the wall. These eventual effects remain currently unknown and deserve further investigations.

Nevertheless, no other works were found that have performed this kind of investigation. How the stress and stretch vary along the wall thickness is important because the wall is actually composed of different layers (Fung, 1993), thus potentially presenting different mechanical properties. Fung (1993), for example, cited some early experimental works with samples of the thoracic aorta of pigs that found that the modulus of Young of the intima and media layers, combined, are as high as four times that of the adventitia. Therefore, the rupture event could

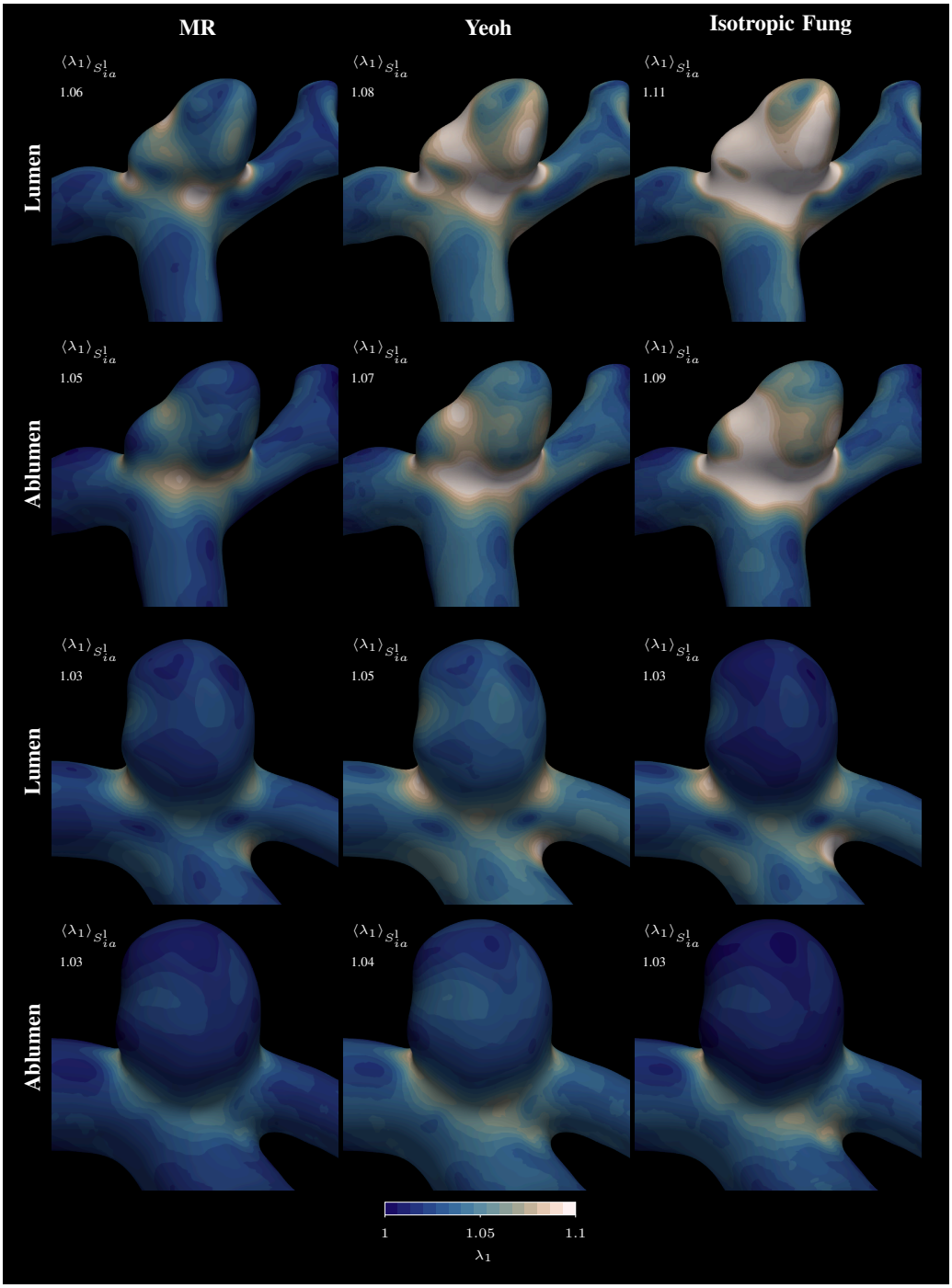

Figure 5. Largest principal stretch field at the peak systole, λ_1, on the luminal and abluminal surfaces of the wall, for the ruptured (top panel) and unruptured (bottom panel) cases, with different hyperelastic laws (columns).

result due to damage in one of the layers, serving as an initial fracture, which would propagate, thus facilitating the complete wall failure.

4. CONCLUSIONS

In this study, we found that different hyperelastic laws produced markedly different stretch fields, possibly explained by the likely higher sensitivity of stretch to the material constants of each law, with the ruptured IA having much larger stretch levels than the unruptured. The same behavior was not encountered for the stress fields in the IA sacs. Additionally, both stress and stretch decreased along the thickness of the wall, indicating that the rupture can start in one of the layers of an IA wall. In practical terms, these findings can help future

researchers to choose a more suitable model to investigate other aspects of the mechanical response of IAs, which can further advance the understanding of the rupture event of an IA.

5. ACKNOWLEDGEMENTS

This research was supported by grants 2017/18514-1 and 2019/19098-7 of the São Paulo Research Foundation (FAPESP). It was also supported by resources supplied by the Center for Scientific Computing (NCC/GridUNESP) of the São Paulo State University (UNESP) (`www2.unesp.br/portal#!/gridunesp`), by ACENET (`www.ace-net.ca`) through Dalhousie University and Compute Canada (`www.computecanada.ca`).

6. REFERENCES

Bazilevs, Y., Hsu, M.C., Zhang, Y., Wang, W., Kvamsdal, T., Hentschel, S. and Isaksen, J.G., 2010a. "Computational vascular fluid-structure interaction: Methodology and application to cerebral aneurysms". *Biomechanics and Modeling in Mechanobiology*, Vol. 9, pp. 481–498. ISSN 16177959. doi:10.1007/s10237-010-0189-7.

Bazilevs, Y., Hsu, M.C., Zhang, Y., Wang, W., Liang, X., Kvamsdal, T., Brekken, R. and Isaksen, J.G., 2010b. "A fully-coupled fluid-structure interaction simulation of cerebral aneurysms". *Computational Mechanics*, Vol. 46, pp. 3–16. ISSN 01787675. doi:10.1007/s00466-009-0421-4.

Brunel, H., Ambard, D., Dufour, H., Roche, P., Costalat, V. and Jourdan, F., 2018. "Rupture limit evaluation of human cerebral aneurysms wall: Experimental study". *Journal of Biomechanics*, Vol. 77, pp. 76–82. ISSN 00219290. doi:10.1016/j.jbiomech.2018.06.016.

Cebral, J.R. and Meng, H., 2012. "Counterpoint: Realizing the Clinical Utility of Computational Fluid Dynamics—Closing the Gap". doi:10.3174/ajnr.a2993.

Cho, K.C., Yang, H., Kim, J.J., Oh, J.H. and Kim, Y.B., 2020. "Prediction of rupture risk in cerebral aneurysms by comparing clinical cases with fluid–structure interaction analyses". *Scientific Reports*, Vol. 10, No. 1, p. 18237. ISSN 2045-2322. doi:10.1038/s41598-020-75362-5.

Costalat, V., Sanchez, M., Ambard, D., Thines, L., Lonjon, N., Nicoud, F., Brunel, H., Lejeune, J.P., Dufour, H., Bouillot, P., Lhaldky, J.P., Kouri, K., Segnarbieux, F., Maurage, C.A., Lobotesis, K., Villa-Uriol, M.C., Zhang, C., Frangi, A.F., Mercier, G., Bonafé, A., Sarry, L. and Jourdan, F., 2011. "Biomechanical wall properties of human intracranial aneurysms resected following surgical clipping (IRRAs Project)". *Journal of Biomechanics*, Vol. 44, No. 15, pp. 2685–2691. doi:10.1016/j.jbiomech.2011.07.026.

Demiray, H., 1972. "A note on the elasticity of soft biological tissues". *Journal of Biomechanics*, Vol. 5, pp. 309–311. doi:10.1016/0021-9290(72)90047-4.

Fung, Y.C., 1993. *Biomechanics - Mechanical Properties of Living Tissues*. Springer New York, New York, NY. ISBN 978-1-4419-3104-7 978-1-4757-2257-4. doi:10.1007/978-1-4757-2257-4.

Hirschhorn, M., Tchantchaleishvili, V., Stevens, R., Rossano, J. and Throckmorton, A., 2020. "Fluid–structure interaction modeling in cardiovascular medicine – A systematic review 2017–2019". *Medical Engineering & Physics*, Vol. 78, pp. 1–13. ISSN 13504533. doi:10.1016/j.medengphy.2020.01.008.

Hoi, Y., Wasserman, B.A., Xie, Y.J., Najjar, S.S., Ferruci, L., Lakatta, E.G., Gerstenblith, G. and Steinman, D.A., 2010. "Characterization of volumetric flow rate waveforms at the carotid bifurcations of older adults". *Physiological Measurement*, Vol. 31, No. 3, pp. 291–302. ISSN 09673334. doi:10.1088/0967-3334/31/3/002.

Holzapfel, G.A., 2000. *Nonlinear Solid Mechanics*. John Wiley & Sons, Inc., Chichester.

Holzapfel, G.A., Gasser, T.C. and Ogden, R.W., 2000. "A new constitutive framework for arterial wall mechanics and a comparative study of material models". *Journal of Elasticity*, Vol. 61, No. 1-3, pp. 1–48. ISSN 03743535. doi:10.1023/A:1010835316564.

Issa, R.I., 1986. "Solution of the implicitly discretised fluid flow equations by operator-splitting". *Journal of Computational Physics*, Vol. 62, No. 1, pp. 40–65. ISSN 10902716. doi:10.1016/0021-9991(86)90099-9.

Jasak, H., 1996. *Error Analysis and Estimation for the Finite Volume Method with Applications to Fluid Flows*. Ph.D. thesis, Imperial College.

Kallmes, D.F., 2012. "Point: CFD—Computational Fluid Dynamics or Confounding Factor Dissemination". *American Journal of Neuroradiology*, Vol. 33, pp. 393–398. doi:10.3174/ajnr.A2993.

Kanyanta, V., Ivankovic, A. and Karac, A., 2009. "Validation of a fluid-structure interaction numerical model

for predicting flow transients in arteries". *Journal of Biomechanics*, Vol. 42, No. 11, pp. 1705–1712. ISSN 00219290. doi:10.1016/j.jbiomech.2009.04.023.

Kanyanta, V., 2009. *Towards Early Diagnosis of Atherosclerosis: Accurate Prediction of Wall Shear Stress*. Ph.D. thesis.

Lee, C.J., Zhang, Y., Takao, H., Murayama, Y. and Qian, Y., 2013. "The influence of elastic upstream artery length on fluid-structure interaction modeling: A comparative study using patient-specific cerebral aneurysm". *Medical Engineering and Physics*, Vol. 35, No. 9, pp. 1377–1384. ISSN 13504533. doi: 10.1016/j.medengphy.2013.03.009.

Liang, L., Steinman, D.A., Brina, O., Chnafa, C., Cancelliere, N.M. and Pereira, V.M., 2019. "Towards the Clinical utility of CFD for assessment of intracranial aneurysm rupture - A systematic review and novel parameter-ranking tool". *Journal of NeuroInterventional Surgery*, Vol. 11, pp. 153–158. ISSN 17598486. doi:10.1136/neurintsurg-2018-014246.

Mooney, M., 1940. "A Theory of Large Elastic Deformation". *Journal of Applied Physics*, Vol. 11, No. 153. doi:10.1063/1.1713863.

Nakagawa, D., Shojima, M., Yoshino, M., Kin, T., Imai, H., Nomura, S., Saito1, T., Nakatomi, H., Oyama1, H. and Saito, N., 2016. "Wall-to-lumen ratio of intracranial arteries measured by indocyanine green angiography". *Asian Journal of Neurosurgery*, Vol. 11, pp. 361–364. doi:10.4103/1793-5482.175637.

Passerini, T., Piccinelli, P., A., V. and Antiga, L., 2021. "aneurisk". `http://ecm2.mathcs.emory.edu/aneuriskweb/index`.

Piccinelli, M., Veneziani, A., Steinman, D.A., Remuzzi, A. and Antiga, L., 2009. "A framework for geometric analysis of vascular structures: Application to cerebral aneurysms". *IEEE Transactions on Medical Imaging*, Vol. 28, No. 8, pp. 1141–1155. doi:10.1109/TMI.2009.2021652.

Ramachandran, M., Laakso, A., Harbaugh, R.E. and Raghavan, M.L., 2012. "On the role of modeling choices in estimation of cerebral aneurysm wall tension". *Journal of Biomechanics*, Vol. 45, No. 16, pp. 2914–2919. ISSN 00219290. doi:10.1016/j.jbiomech.2012.07.029.

Sacks, A.H. and Tickner, E.G., 1968. "The compressibility of blood". *Biorheology*, Vol. 5, No. 4, pp. 271–274. ISSN 18785034, 0006355X. doi:10.3233/BIR-1968-5403.

Sanchez, M., Ecker, O., Ambard, D., Jourdan, F., Nicoud, F., Mendez, S., Lejeune, J.P., Thines, L., Dufour, H., Brunel, H., Machi, P., Lobotesis, K., Bonafe, A. and Costalat, V., 2014. "Intracranial aneurysmal pulsatility as a new individual criterion for rupture risk evaluation: Biomechanical and numeric approach (IRRAs Project)". *American Journal of Neuroradiology*, Vol. 35, pp. 1765–1771. doi:10.3174/ajnr.A3949.

Saqr, K.M., Rashad, S., Tupin, S., Niizuma, K., Hassan, T., Tominaga, T. and Ohta, M., 2019. "What does computational fluid dynamics tell us about intracranial aneurysms? A meta-analysis and critical review". *Journal of Cerebral Blood Flow and Metabolism*, Vol. 0, No. 0, pp. 1–19. doi:10.1177/0271678X19854640.

Torii, R., Oshima, M., Kobayashi, T., Takagi, K. and Tezduyar, T.E., 2006. "Fluid-structure interaction modeling of aneurysmal conditions with high and normal blood pressures". *Computational Mechanics*, Vol. 38, pp. 482–490. ISSN 01787675. doi:10.1007/s00466-006-0065-6.

Torii, R., Oshima, M., Kobayashi, T., Takagi, K. and Tezduyar, T.E., 2008. "Fluid-structure interaction modeling of a patient-specific cerebral aneurysm: Influence of structural modeling". *Computational Mechanics*, Vol. 43, pp. 151–159. ISSN 01787675. doi:10.1007/s00466-008-0325-8.

Torii, R., Oshima, M., Kobayashi, T., Takagi, K. and Tezduyar, T.E., 2010. "Influence of wall thickness on fluid–structure interaction computations of cerebral aneurysms". *International Journal for Numerical Methods in Biomedical Engineering*, Vol. 26, pp. 336–347. ISSN 20407939. doi:10.1002/cnm.

Valencia, A., Burdiles, P., Ignat, M., Mura, J., Bravo, E., Rivera, R. and Sordo, J., 2013. "Fluid structural analysis of human cerebral aneurysm using their own wall mechanical properties". *Computational and Mathematical Methods in Medicine*, Vol. 2013, pp. 1–18. ISSN 1748670X. doi:10.1155/2013/293128.

Valencia, A., Muñoz, F., Arayaa, S., Rivera, R. and Bravo, E., 2009. "Comparison between computational fluid dynamics, fluid-structure interaction and computational structural dynamics predictions of flow-induced wall mechanics in an anatomically realistic cerebral aneurysm model". *International Journal of Computational Fluid Dynamics*, Vol. 23, No. 9, pp. 649–666. ISSN 10618562. doi:10.1080/10618560903476386.

Vlak, M.H.M., Rinkel, G.J.E., Greebe, P. and Algra, A., 2013. "Risk of rupture of an intracranial aneurysm based

on patient characteristics: A case-control study". *Stroke*, Vol. 44, No. 5, pp. 1256–1259. ISSN 00392499. doi:10.1161/STROKEAHA.111.000679.

Zarrinkoob, L., Ambarki, K., Wåhlin, A., Birgander, R., Eklund, A. and Malm, J., 2015. "Blood flow distribution in cerebral arteries". *Journal of Cerebral Blood Flow and Metabolism*, Vol. 35, pp. 648–654. ISSN 15597016. doi:10.1038/jcbfm.2014.241.

7. RESPONSIBILITY NOTICE

The authors are solely responsible for the printed material included in this paper.